Volume 5
Number 9
September 2025
Pages 935–1064

Environmental Science
Atmospheres

rsc.li/esatmospheres

ISSN 2634-3606

ROYAL SOCIETY OF CHEMISTRY

PAPER

Hendryk Czech *et al.*

Emission speciation of volatile and intermediate volatility organic compounds from a marine engine: effect of engine load, fuel type and photochemical aging

Environmental Science: Atmospheres

ROYAL SOCIETY OF CHEMISTRY

PAPER

View Article Online
View Journal | View Issue

Cite this: *Environ. Sci.: Atmos.*, 2025, **5**, 973

Emission speciation of volatile and intermediate volatility organic compounds from a marine engine: effect of engine load, fuel type and photochemical aging

Deeksha Shukla,[ab] Hendryk Czech,*[ab] Tuukka Kokkola,[c] Martin Bauer,[b] Andreas Paul,[bd] Uwe Etzien,[e] Mika Ihalainen,[c] Zheng Fang,[f] Anni Hartikainen,[c] Nadine Gawlitta,[aj] Thorsten Hohaus,[d] Yinon Rudich,[f] Thorsten Streibel,[ab] Bert Buchholz,[e] Olli Sippula,[cg] Johan Øvrevik,[hi] Jürgen Schnelle-Kreis[a] and Ralf Zimmermann[ab]

The enforcement of global fuel sulfur content (FSC) regulations has significantly reduced SO_2 and particulate matter (PM) emissions from ships. However, the impact of the International Maritime Organization's (IMO) sulfur reduction policy on gaseous hydrocarbon emissions, including volatile and intermediate volatility organic compounds (VOCs/IVOCs), remains underexplored. In this study, a 4-stroke single cylinder marine engine was operated using marine gas oil (MGO, FSC = 0.01%) and low-sulfur heavy fuel oil (LS-HFO, FSC = 0.5%) across various engine loads, ranging from 20 kW to a maximum of 80 kW. Emissions were photochemically aged in the oxidation flow reactor "PEAR," simulating an equivalent photochemical aging period from 1.4 ± 0.2 to 4.6 ± 0.8 days related to the OH· exposure. Emission factors (EFs) of all targeted VOCs/IVOCs varied significantly, ranging from 20.0 ± 2.5 to 180 ± 20 mg kWh^{-1} and from 26.0 ± 11.0 to 280 ± 100 mg kWh^{-1} from a high (80 kW) to low engine load (20 kW) for MGO and LS-HFO, respectively. Monoaromatics dominated total fresh emissions for MGO (64%) and LS-HFO (76%), followed by alkanes. Naphthalene and alkylated naphthalene content declined more than monoaromatic and alkane content, thus changing the VOC/IVOC emission pattern after photochemical aging. Estimated SOA from targeted VOC/IVOC precursors accounted for 41% of the measured secondary organic aerosol (SOA) for MGO, while a lower contribution (34%) was observed for LS-HFO at 20 kW engine load, highlighting the role of unmeasured VOCs/IVOCs in SOA formation. Expanding the research on the effects of atmospheric aging on marine emissions will offer valuable insights into this underexplored area.

Received 2nd April 2025
Accepted 29th July 2025

DOI: 10.1039/d5ea00040h

rsc.li/esatmospheres

Environmental significance

The International Maritime Organization's (IMO) sulfur reduction policy has successfully lowered sulfur dioxide (SO_2) and particulate matter (PM) emissions from shipping, yet its impact on gaseous hydrocarbon emissions remains poorly understood. This study reveals that volatile and intermediate-volatility organic compound (VOC/IVOC) emissions from marine engines are influenced by fuel type and engine load: atmospheric processing significantly alters the VOC/IVOC composition, leading to secondary organic aerosol (SOA) formation. A substantial fraction of SOA remains unexplained by common measured SOA precursors, emphasizing the need for a broader characterization of VOC/IVOC emissions. As maritime traffic continues its transition toward low-sulfur fuels, understanding the full range of emissions and their atmospheric transformations is critical for accurately assessing air quality and climate impacts.

[a]*Cooperation Group, "Comprehensive Molecular Analytics", Helmholtz Zentrum München, Neuherberg, 85764, Germany. E-mail: hendryk.czech@uni-rostock.de*
[b]*Department of Analytical and Technical Chemistry, University of Rostock, Rostock, 18059, Germany*
[c]*Department of Environmental and Biological Science, University of Eastern Finland, Kuopio, 70210, Finland*
[d]*Institute of Climate and Energy Systems, ICE-3: Troposphere, Forschungszentrum Jülich GmbH, Jülich, 52428, Germany*
[e]*Department of Piston Machinery and Internal Combustion Engines, University of Rostock, Rostock, 18059, Germany*
[f]*Department of Earth and Planetary Sciences, Weizmann Institute of Science, Rehovot, Israel*
[g]*Department of Chemistry, University of Eastern Finland, Joensuu, 80101, Finland*
[h]*Norwegian Institute of Public Health, N-0213 Oslo, Norway*
[i]*Department of Biosciences, University of Oslo, N-0213, Norway*
[j]*Department of Plant and Environmental Sciences, Faculty of Science, University of Copenhagen, 1871 Frederiksberg C, Denmark*

1 Introduction

Globalization has accelerated international trade, with maritime transport serving as an essential foundation, accounting for over 80% of the total global merchandise trade.[1] It is predicted to triple by 2050.[2] However, this comes with significant environmental and public health impacts.[3] Since a substantial number of marine emissions occur within the 400 km of coastlines, it has significantly contributed to environment-related diseases in coastal areas.[4,5] Research suggests that prior to 2020, global shipping may have been responsible for up to 400 000 annual premature deaths,[6] with highest mortality rates near coastlines in North America, Europe, and East Asia.[7] Marine-engine emissions have been shown to cause oxidative stress, inflammation, and disruption of cellular metabolism[8] and have been associated with a wide range of health risks, including lung cancer, cardiovascular, and pulmonary diseases.[9,10] Marine engines generate numerous particulate and gaseous air pollutants, including SO_x, NO_x, particulate matter (PM), greenhouse gases, and non-methane volatile organic compounds (NMVOCs), along with short-lived climate forcers.[11,12] The aerosol emissions directly and indirectly affect the atmospheric light scattering and absorbing properties with a net positive radiative forcing contributing to climate change.[6] Global shipping emitted 16.7–20 Mt NO_x, 9.6–10.9 Mt SO_x, and nearly 5.3 Mt NMVOC in 2018, accounting for 16.8% of NO_x, 9.2% of SO_x, and 4% of NMVOC emissions from all anthropogenic sources.[13] These NMVOCs are oxidized in the atmosphere, condensate as secondary organic aerosol (SOA) to the particle phase, and become further processed in multiphase aging.[14]

In order to reduce the significant health and climate impacts caused by marine emission, the International Maritime Organization (IMO) established emission control areas (ECA) to directly reduce SO_x and NO_x and indirectly reduce PM emissions in the Baltic Sea, the North Sea and English Channel, North America (except the Arctic), and U.S. Caribbean Sea. As a recent prevention measure, IMO also applied a global sulfur cap on January 1, 2020, requiring all ships to use fuels with a fuel sulfur content (FSC) of <0.5% by mass,[15] which leads to low sulfur fuels dominating the worldwide maritime consumption.[15] The IMO has also set regional emission control areas for SO_x (SECA, 0.1% sulfur limit in 2015) and NO_x (NECA, effective from 2021 for new builds). In accordance with the compliance, ship owners can either switch to low-sulfur fuels such as marine gas oil (MGO) or low sulfur heavy fuel oil (LS-HFO), or install an abatement system ("sulfur scrubbers"), allowing them to use bunker fuel oils in SECA.[16] According to IMO, SO_x emissions from shipping were expected to decline by over 75% following the sulfur cap implementation.[17] In agreement with this, recent studies have indicated that the transition to low-sulfur fuels led to a reduction of criteria pollutants in direct emissions, *i.e.*, SO_x, NO_x and PM.[18,19] However, the impact of low-sulfur fuels on organic vapors including VOCs (effective saturation concentration $C^* > 10^6$ μg m^{-3})[20] and IVOCs (effective saturation concentration C^* between 10^3 and 10^6 μg m^{-3})[21] remains to be determined. Notably, a recent study reported a dramatic 15-fold increase in emissions of aromatic gaseous species in coastal vessels after fuel-switch policy, due to the replacement from high-sulfur residual oil with low sulfur diesel oil.[22]

Aromatic VOCs and IVOCs serve as potential precursors for secondary particle formation, contributing to air pollution. These gaseous precursors are repeatedly proven to be a key contributor to SOA,[23] and are closely associated with elevated ground level ozone concentrations, especially in coastal regions.[11] Despite this significant impact, relatively few studies have investigated emissions of VOCs/IVOCs from marine engines and assessed their potential to form SOA, *e.g.*, depending on fuel type. It has been indicated that the regulations mandating low-sulfur fuel-use may unintentionally increase SOA formation, despite reductions in primary organic aerosol (POA) emissions.[24] This highlights the need for a more in-depth investigation of VOC emissions and their SOA formation potential under current fuel regulations. Engine conditions also largely determine the overall emission with substantially higher emissions observed at ground idle or low load operations.[21,25]

In our study, we investigated the emission speciation of gaseous fractions from a marine engine running on LS-HFO and MGO with different engine operating conditions under laboratory conditions, and further explored the effects of photochemical aging using "Photochemical Emission Aging flow tube Reactor'' (PEAR),[26] a high-volume oxidation flow reactor (OFR). The changes in VOC and OA composition after laboratory-photochemical aging were characterized, and the SOA formation potentials from the photochemical oxidation of various SOA precursors were estimated and further compared to the measured SOA. Our findings provide new insights into the complex dynamics of marine emissions and their atmospheric transformation.

2 Materials and methods

2.1 Test engine, fuels, operating and aging conditions

A single-cylinder four-stroke marine engine was operated (according to the test cycle E2 of ISO 8178) on either MGO (FSC = 0.01 S% m m^{-1}) or LS-HFO (FSC = 0.5 S% m m^{-1}) over distinct phases of engine cycle across 20 kW (25% of nominal load), 40 kW, 60 kW and 80 kW (100% nominal load). The engine loads were run for 15%, 15%, 50% and 20% of the whole 2-hour cycle time. Previous studies[12,27,28] have provided detailed insights into the engine characteristics, and demonstrated its suitability as model for larger marine engines. Relevant engine and fuel specifications from this study are documented in Tables S1 and S2.

Raw exhaust emissions were directed through a heated precyclone (400 °C) and heated lines maintained at 350 °C. A two-stage dilution and sampling setup (DAS, Venacontra, Finland) consisting of a porous tube diluter (PTD), followed by an ejector diluter (ED), was used to achieve a dilution ratio of 1 : 100. The dilution was controlled by an automated dilution system, which continuously monitored CO_2 concentrations in the sample before and after dilution, as well as in the clean air used for the dilution. The exhaust samples after 100-fold

dilution were channeled through the PEAR for laboratory-photochemical aging across different loads at a reactor flow rate of 100 L min^{-1} with an average residence time of 70 seconds. Prior to entering the PEAR, the diluted exhaust was mixed with ozone (Ozone Generator Model 1000; Jelight Co) and water vapor to achieve 10 ppm of ozone and 50% relative humidity (humidifier Model 125-240-5MP, Perma Pure, Ltd, USA), respectively.

Inside the PEAR, the ozone was photolyzed by UV light at a wavelength of 254 nm, and the resulting singlet oxygen ($O(^1D)$) reacted with water vapor to form OH·, which initiated the oxidation of the engine exhaust. The OH· exposure was estimated using the decay of deuterated butanol (butanol-d9, m/z 66.12) measured by proton transfer reaction-time of flight-mass spectrometry (PTR-TOF-MS-8000, Ionicon, Austria).[29] The reaction rate constant for OH· and butanol-d9 was adopted from a previous measurement.[30] The OH· exposures are presented as atmospheric equivalent (equiv.) aging days, assuming an ambient OH· concentration of 1.0×10^6 molecules cm^{-3}. The photochemical aging days varied across engine loads from 1.4–3.8 equiv. days for MGO and 2.2–4.6 equiv. days for LS-HFO, and were higher at lower (20 and 40 kW) engine loads. Further details on photochemical age are documented in Table S3.

2.2 Sampling and analyses

The schematic of the experimental setup is depicted in Fig. 1. The main exhaust gas components (NO, NO_2, CO and SO_2) were monitored from the raw undiluted flue gas using Fourier-transform infrared spectroscopy (FTIR DX4000, Gasmet Technologies, Finland). Sampling was carried out undiluted with sampling rates of 3 L min^{-1} by a 5 m heated transfer line (Winkler GmbH, Heidelberg, Germany). A portable gas sample probe (PSP4000-H, M&C, Germany) containing the filter heated to 180 °C was installed upstream of the heated transfer line. The software Calcmet (Gasmet, Vantaa, Finland) was used for spectrum analysis, including the blank subtraction to acquire the absorbance of the sampled gaseous compounds and to correct the baseline absorbance.

Gas phase organics for offline targeted analysis were collected with adsorber tubes consisting of three sublayers of graphitized carbon black (GCB) sorbents intended to capture compounds across a wide range of volatilities (Table S4). Quartz fiber filters (QFFs) (10 mm) were installed as a pre-filter in a stainless-steel filter holder assembly, positioned between an empty glass tube upstream and adsorber tube downstream, to remove particulate fractions (Fig. S1), as previously described in Mason *et al.* (2020).[31] Seven sets of composite samples were collected for MGO and LS-HFO for offline analysis in fresh and aged conditions. Each set of samples consisted of 8 adsorber tubes over 20 kW, 40 kW, 60 kW and 80 kW engine loads. Sampling was conducted for 10 min at a flow rate of 1 L min^{-1}, accounting for a total sampling volume of 10 L. All collected samples were stored at −20 °C until analysis.

The analysis of adsorber tubes was carried out using gas chromatography mass spectrometry (Shimadzu GCMS-QP2010 Ultra, Japan) coupled to a thermal desorption unit (Shimadzu TD-20, Japan). The separation took place on a VF-xMS, high-arylene-modified phase column (30 m + 5 m pre-column, 0.25 mm ID × 0.25 μm df, Agilent Varian, USA). Detailed information regarding sampling and analysis parameters for the collected gas phase adsorber tubes is documented in Tables S5–S8 and Fig. S2, respectively.

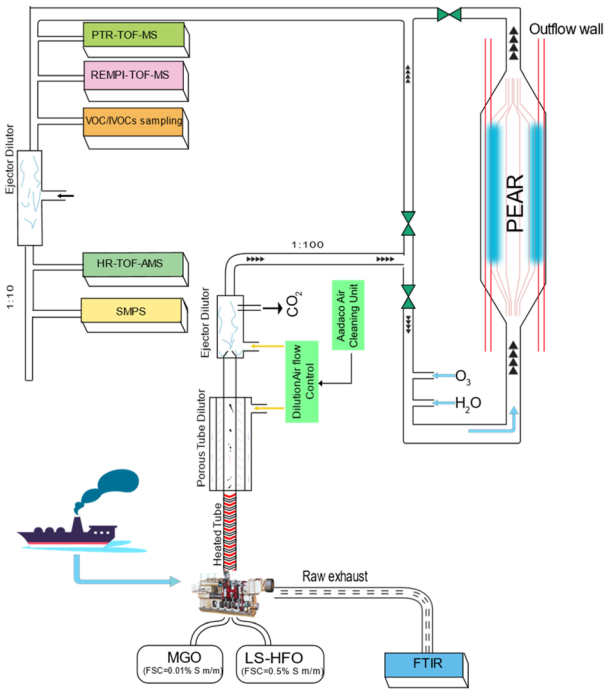

Fig. 1 Schematic of the sampling and measurement setup for the investigation of ship emission utilizing marine fuel MGO (FSC = 0.01%) and LS-HFO (FSC = 0.5%). Instruments in-use are FTIR (Fourier-transform infrared spectroscopy), PTR-TOF-MS (proton transfer reaction-time of flight-mass spectrometry), HR-TOF-AMS (high resolution-time of flight-aerosol mass spectrometer), SMPS (scanning mobility particle sizer), REMPI TOF-MS (resonance enhanced multi-photon ionization time of flight mass spectrometry), VOC/IVOC (volatile organic compounds/intermediate volatility organic compounds) sampling system, and PEAR (Photochemical Emission Aging flow tube Reactor). A dilution of 1 : 100 was channeled through PEAR; further, 1 : 10 dilution (total 1 : 1000) was performed for the investigation of aerosol particle phase, and an additional 3-fold dilution was performed during aged LS-HFO experiments.

Online analysis of aromatic VOCs/IVOCs in fresh and aged emissions was performed using an untargeted resonance-enhanced multiphoton ionization (REMPI) time-of-flight mass spectrometer (TOF-MS; PHOTO-TOF, Photonion GmbH, Germany). Fresh or aged exhaust gas samples were introduced through a stepwise-heated capillary (150 °C/200 °C/225 °C, ID = 200 μm). To prevent particles from entering the TOF-MS, a glass fiber filter was installed at 200 °C. Within the ion source, the exhaust gas components were exposed to laser radiation at 248 nm, generated by a KrF laser (PhotonEx 200; MLase GmbH, Germany) operating at a repetition rate of 200 Hz and a pulse energy of 4 mJ. Aromatic VOCs with ionization energies below 10 eV and long-lived transition states were selectively ionized *via* a two-photon REMPI process utilizing laser light of 248 nm.[32]

The exhaust was subjected to an additional ejector diluter (Palas GmbH, Germany) for further 10-fold dilution before online instrumentation (total dilution = 1 : 1000) used for the investigation of the aerosol particle phase. During aged LS-HFO experiments, an additional 3-fold dilution was placed before the high-resolution time-of-flight aerosol mass spectrometer (HR-TOF-AMS; Aerodyne Inc., USA).[33] The HR-TOF-AMS was utilized to quantitatively determine the chemical composition of the non-refractive aerosol, where measurements were performed at 1-min intervals with 30 seconds dedicated to V-mode (mass resolution of 2.1×10^3 (at m/z 200)) and 30 seconds for particle time of flight-mode (PTOF-mode). The critical orifice allowed for the measurement of particles in the size range of 42 nm to 645 nm. Ionization efficiency and relative ionization efficiency calibrations with ammonium nitrate and ammonium sulfate, respectively, were performed weekly to ensure data quality.[34] All data were evaluated based on the ionization efficiency calibration determined on a given week. Furthermore, during each experiment, a 10-minute sample was taken through a HEPA filter to get an accurate CO_2 background measurement. Further instrument specifications can be found in Hartner *et al.* (2022).[35] A scanning mobility particle sizer (SMPS, TSI Incorporated Type 3082, USA) was utilized for particle size distribution and number concentration in individual loads for before and after aging experiments.

2.3 Quantification and data evaluation

VOCs/IVOCs were analyzed and quantified by targeted TD-GCMS and untargeted REMPI-TOF-MS. The quantification of a total of twenty-six individual compounds belonging to different classes of volatile organics, *i.e.*, mono-aromatics, polycyclic aromatic hydrocarbons (PAHs) and alkylated PAHs and straight chain (*n*-)alkanes, was done using an isotope-labeled authentic internal standard and a calibration standard mixture using TD-GCMS. Shimadzu GCMSsolution Ver.2 software was utilized to perform data acquisition and processing for peak identification and quantification. Data processing parameters are documented in Table S9. A mass spectral comparison was performed using the NIST library (version 2.3, 2017). In REMPI, the signals of ions detected by the Reflectron TOF-MS were converted to m/z by in-house MATLAB scripts (R2024a; MathWorks, Inc., USA). REMPI-TOFMS provides quantitative data on C3- and C4-naphthalenes, C1–C3 phenanthrenes, benzene, and toluene, complimentary to the results from TD-GCMS. Further details on the quantification methodology and associated limitations are provided in the SI Text S1. AMS data were treated in the TOF-AMS Analysis Toolkit 1.65 (SQUIRREL), and HR analysis was performed with the TOF-AMS HR Analysis 1.25 (PIKA), both operated in IGOR Pro 8.0.4.2. SMPS data were treated with AIM V.10.3.1.0. software.

The emission factor (EF) in terms of power consumed (mg kWh^{-1}) was calculated based upon the fuel consumption of the engine over each engine load, as per eqn (1):

$$EF_i = \frac{C_i \times V_{nEG}}{P_{engine}} \quad (1)$$

where EF_i is the emission factor for the pollutant (i) in mg kWh^{-1}, C_i = concentration of the pollutant (i) in the exhaust gas in mg m^{-3}, V_{nEG} is the volumetric flow rate of the exhaust gas in $m^3\ h^{-1}$, and P_{engine} is the power output of the engine in kW. The resulting conversion factors from concentrations to mg kWh^{-1} of power consumed and also to mg kg^{-1} fuel burnt are provided in Table S10.

POA was determined based upon the organic fraction from the fresh emissions (no aging), and the SOA fraction was determined by any increase from the POA for the given fuel, as per eqn (2):

$$SOA_x = OA_x - POA \quad (2)$$

where SOA_x is the SOA mass formed after x days of aging, OA_x is the total organic mass measured after a simulated age of x days, and POA is the total organic mass at 0 days of age.

The bottom-up estimation (*i.e.*, VOCs oxidation yield method), similarly as used in Hartikainen *et al.* (2024),[36] was used to calculate the SOA formation potential, SOAFP (in mg kWh^{-1}) from the VOCs/IVOCs, as per eqn (3):

$$SOAFP = \sum_i (EF_i \times Y_i) \quad (3)$$

where Y_i is the SOA yield for VOC species based upon the previously published literature. This method accounts for traditional SOA precursors and provides an estimate of their contributions, either as individual compounds or compound classes. The estimated SOA is further compared to the measured SOA to evaluate how well the identified VOCs/IVOCs can explain the actual SOA formation at each load. Further details on Y_i values are provided in the SI Text S2.

A two-sample t-test was used to compare the mean EF of fresh and aged emission. Mean EF were considered as significantly different at a significance level of 0.05. Bonferroni correction was applied to adjust the p-values from multiple testing of individual emission components. The fold changes and p-values are listed in Tables S11 and S12, respectively.

To evaluate the consistency of TD-GCMS and REMPI-TOFMS, Deming regression was performed on the mutual analytes naphthalene, C1-naphthalene (sum of 1- and 2-methylnaphthalene) and phenanthrene (Fig. S3).

Principal Component Analysis (PCA) was applied to explore the relationship between the VOCs/IVOCs emission profile and associated factors, such as the fuel-type, engine load, photochemical aging and the contributions of specific compounds to overall variability. The results and detailed discussion of the PCA are presented in subsequent sections. All the statistical analyses were performed in Spyder 5.1.5 (Python version 3.9.7 64-bit) software at $\alpha = 0.05$.

2.4 Quality assurance and quality control

Rigorous quality assurance and control measures were maintained during the complete experiments. Adsorber tubes were conditioned under a protective nitrogen atmosphere at 350 °C for 1 h, 30 min to get rid of potential contaminants prior to sampling. The recovery of VOCs/IVOCs during analysis was

calculated using deuterated standards that were spiked into each adsorber tube prior to thermal desorption, and the recovery rates ranged in between 85-110% (Table S13). The calibration standard working curve of each target compound showed a good linear response, and all the linear correlation coefficients were >0.99 (Table S14).

3 Results and discussion

3.1 Primary gaseous emission speciation from marine engine: effect of engine load and fuel-type

The EFs of raw exhaust gas components NO_x (NO + NO_2), SO_2, and CO are presented in Fig. 2 and Table S15. MGO and LS-HFO fuel combustion resulted in comparable levels of NO_x emissions. Internal combustion engines (T > 2500 K) generate thermal NO_x from combustion air *via* N_2+O_2, which outweighs fuel-NO_x[37] and explains similar NO_x emissions from both the fuels. Additionally, the timing of the fuel-injection and crank angle plays an important role in NO_x formation, as early injection (low crank angle) allows for longer residence time for combustion, favoring thermal NO_x, while late injection leads to insufficient fuel oxidation due to shorter residence time, leading to enhanced soot emissions.[38] The weighted average NO_x emissions comply with Tier II of the MARPOL Annex VI (8.2 g kWh^{-1}, n = 1500 rpm); however, they do not comply with Tier III (2.1 g kWh^{-1}, n = 1500 rpm) of the nitrogen emission control areas (NECA).

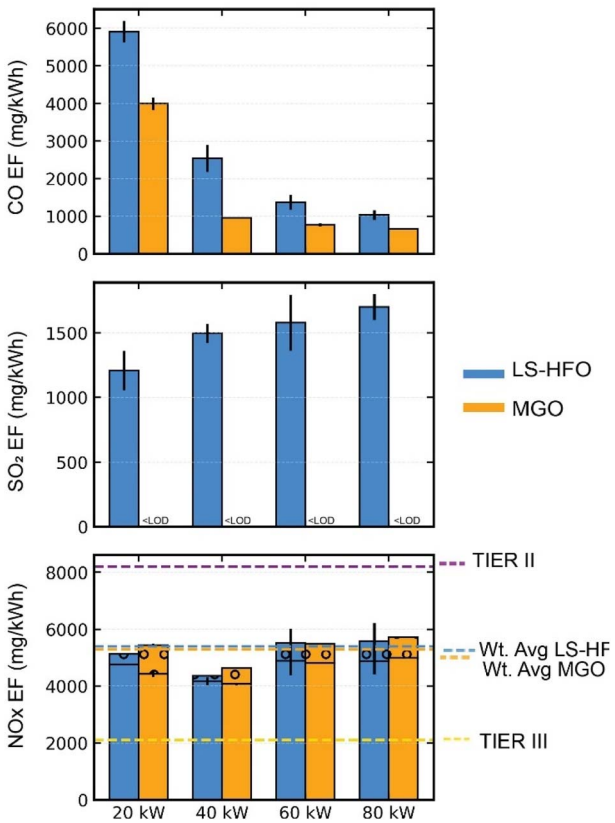

Fig. 2 Emission factors (EFs, mg kWh^{-1}) of raw exhaust gases CO, SO_2, and NO_x (NO + NO_2) over different engine loads for MGO and LS-HFO (arithmetic mean ± standard deviation). The dashed lines in the lowest panel indicate the Tier II and III levels established by MARPOL VI Annex, as per IMO regulation. Revolution (n) = 1500 rpm has been taken during the calculation for these values. The dashed lines in the center represent the weighted average for the cycle, where 20-, 40-, 60- and 80 kW engine loads were run for 15%, 15%, 50% and 20% of the whole cycle time (2 hours), respectively (n = 3 at each load for both MGO and LS-HFO).

The emissions of SO_2 and CO were directly influenced by changing the engine operating conditions and fuel-type (Fig. 2). Switching from HFO (FSC = 0.5% m m^{-1}) to low-sulfur MGO (FSC = 0.01% m m^{-1}) provided large reductions in SO_2 emissions, while SO_2 emissions from HFO exceeded 1000 mg kWh^{-1} for all engine loads. The corresponding emissions from MGO were below detection limits. Contrary to SO_2 emissions, CO emissions declined linearly with engine load, indicating improved combustion efficiency at higher engine loads, which was in line with previous studies.[11,28] At lower loads, the fuel feeding rate is reduced, which affects the air-to-fuel ratio. Higher excess air results in lower combustion temperatures and less effective fuel conversion, leading to elevated CO emissions at low load conditions.

A total of thirty-three VOCs/IVOCs, including mono-aromatics, low molecular-weight (two-three ring) PAHs and alkylated PAHs, and *n*-alkanes were identified and quantified in the ship exhaust samples using authentic standards by TD-GCMS and/or semi-quantified by REMPI-TOF-MS (Fig. 3). Emission factors (EFs) of all targeted VOCs/IVOCs varied significantly, ranging from 20.0 ± 2.5 to 180 ± 20 mg kWh^{-1} and from 26.0 ± 11.0 to 280 ± 100 mg kWh^{-1} from high (80 kW) to low engine load (20 kW) for MGO and LS-HFO, respectively, appearing within the range reported from different cargo ships and ocean-going vessels (OGVs) in a recent study.[39] HFO is produced from blending the vacuum residue of crude oil distillation with middle distillate, *i.e.*, a diesel-like fuel. Therefore, apart from sulfur-containing species, a similar composition of the volatile fraction is expected, though variations are caused by the molecular composition of the crude oil and specific steps in refining. For example, a study on large cargo vessels operated under real-world conditions reported that the emissions were enhanced by a factor of 2.4 after the fuel-switch,[40] whereas another study on Chinese OGVs reported that the emissions were reduced by a factor of 3.4, when switched from high- to low-sulfur fuel.[41] In the present study, the operational mode of the engine largely influenced the emissions for both fuels, which was consistent with previous studies.[25,42] The smallest EFs were observed at 80 kW, which constituted only ~11% and ~30% of the EFs at 20- and 40-kW engine load for MGO, and ~9% and 39% of the EFs at 20- and 40-kW engine load for LS-HFO. Fuel-type had little influence on the emissions of VOCs/IVOCs, except for mono-aromatics such as benzene and toluene, which were present in higher concentrations in LS-HFO emissions (Fig. 3) compared to MGO.

Among the analytical targets, the predominant mass fraction was attributed to monoaromatics, accounting for 64% and 76% contribution of the total identified volatile emissions in the ship exhaust tested herein, for MGO and LS-HFO, respectively. In particular, benzene, toluene and xylenes (BTX) were the dominating compounds, which is in line with a study by Huang *et al.*

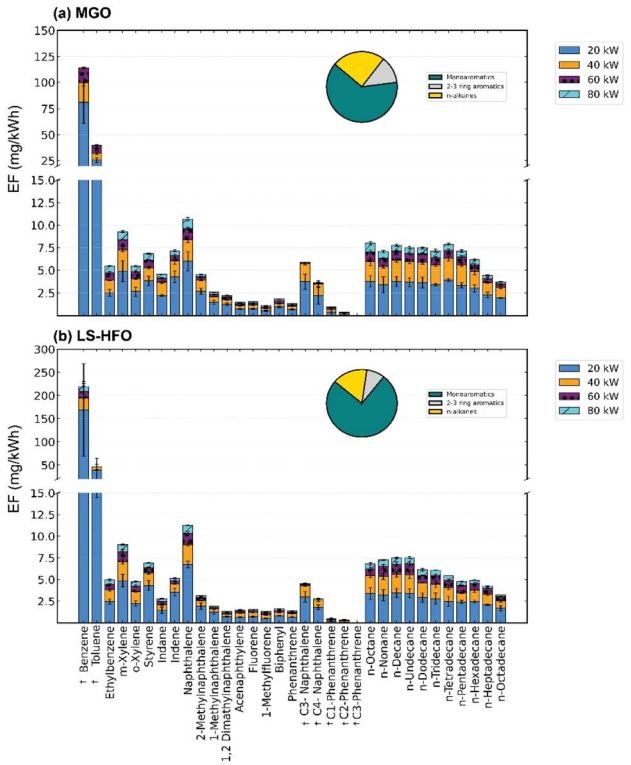

Fig. 3 Total emission factors (EFs, mg kWh^{-1}) of VOCs/IVOCs over 20-, 40-, 60- and 80 kW engine loads for (a) MGO and (b) LS-HFO (arithmetic mean ± standard deviation). Pie charts on the top of each stacked bar chart represent the mass fraction contribution (%, for the cycle of 2 hours) of different classes, such as *n*-alkanes (C8–C18), monoaromatics, and 2–3 ring aromatics. Compounds with dagger symbol (†) were measured with REMPI-TOFMS. Error bars indicate the standard deviation between replicates ($n \geq 3$ for each 20-, 40-, 60 kW, and 80 kW for MGO and $n = 3$ for 20-, 40- and 60 kW and $n = 2$ for 80 kW for LS-HFO for compounds measured *via* TD-GCMS compounds and $n = 3$ for MGO and $n = 2$ for LS-HFO) at each load for compounds measured *via* REMPI-TOF-MS.

(2018),[11] indicating ~50–74% contribution from single ring aromatics in various samples in the tested ship exhaust. Aliphatic *n*-alkanes (C8–C18) accounted for both 24% for MGO and 16% for LS-HFO of the total analyzed species.

Regardless of the fuel type, naphthalene and up to C4-alkylated naphthalenes (m/z = 128, 142, 156, 170, and 184) were detected as prominent emission constituents. A previous study[43] focused on chemometric analysis of ship emissions also highlighted that the alkylated pattern of aromatic structures with one to three rings serve as a discriminator between ship and land-based emissions. The two primary processes responsible for the formation of PAHs are direct emission of unburnt fuel components and pyrosynthesis, which involves the formation of aromatics through the regeneration of fragmented radical species.[44] The optimized engine conditions in this study resulted in relatively lower total EFVOCs as compared to those reported in the literature.[45–47] However, these differences can be attributed to variations in the engine type, specifically whether the engine is a two-stroke or a four-stroke engine. Two stroke engines usually have lower load dependence, and generally produce higher THC emissions compared to four-stroke engines. In addition, different fuel composition and differences in the sampling, operating conditions and different VOC targets may also contribute to variation in emissions.

3.2 Effect of photochemical aging on marine engine emissions

The effects of photochemical aging on emissions from low (20 kW) and high (60 kW) engine loads for both MGO and LS-HFO were investigated for contrasting maneuvering activities. Fig. 4 shows a more intense degradation of VOCs/IVOCs 20 kW engine load compared to 60 kW for both MGO and LS-HFO. However, the effect of aging varied for individual VOC because of their different rate constants towards OH·.[48] With REMPI-TOF-MS, compounds after aging were detected, but their quantification was not possible (see SI Text S1). The discussion herein focuses on the effect of aging for VOCs/IVOCs quantified using TD-GCMS. Across all the VOCs/IVOCs categories of compounds measured with TD-GCMS, naphthalene and alkylated naphthalenes (m/z = 128, 142, 156) were affected the most by photochemical aging (3.5–4.6 equiv. days) at low engine loads for both MGO and LS-HFO. For example, at 20 kW, naphthalene degraded by 85–89% after aging, but to a lower extent of ~40% for MGO and LS-HFO at 60 kW engine load. This observation may be explained by the higher concentration of NO_x in the emission at higher engine loads, having a higher rate constant with OH· than organic species and increasing the total OH· reactivity of the emissions. Naphthalene is the most abundant PAH in the atmosphere and contributes to SOA formation OH-driven oxidation.[49] Although less abundant, PAHs contributed 3–5 times more to SOA than monoaromatics and accounted for up to 54% of SOA formed from diesel exhaust, as found by Chan *et al.* (2009).[50] Monoaromatics and *n*-alkanes were also significantly affected by photochemical processing, with >70% reduction in aged exhaust at 20 kW engine load for both MGO and LS-HFO. However, the emission reduction was limited to 25–30% for alkanes and ~35% for monoaromatics at 60 kW engine load.

Very few studies have investigated the aging effects of ship emissions. A recent study by Paul *et al.* (2025)[51] focusing on the photochemical aging of ship emissions over a period of 0–9 days found that SOA formation peaked at 3.3 days, while secondary sulfate formation reached its maximum at nearly 9 days of equiv. photochemical aging. This indicates that the formation dynamics of each aerosol type are influenced by distinct atmospheric aging processes. Another study focusing on real-world emissions of ship equipped with diesel oxidation catalyst and a scrubber[52] reported no secondary particle formation after OFR aging, possibly because the precursors were effectively removed by the exhaust after-treatment technology. For the first time, the SOA formation from a marine engine across different engine loads was observed in a laboratory-aging experiment. Precursors were consumed and rapidly formed SOA with the initiated photochemistry in the OFR. In addition to lower engine loads (20- and 40-kW), SOA formation at higher engine loads (60- and

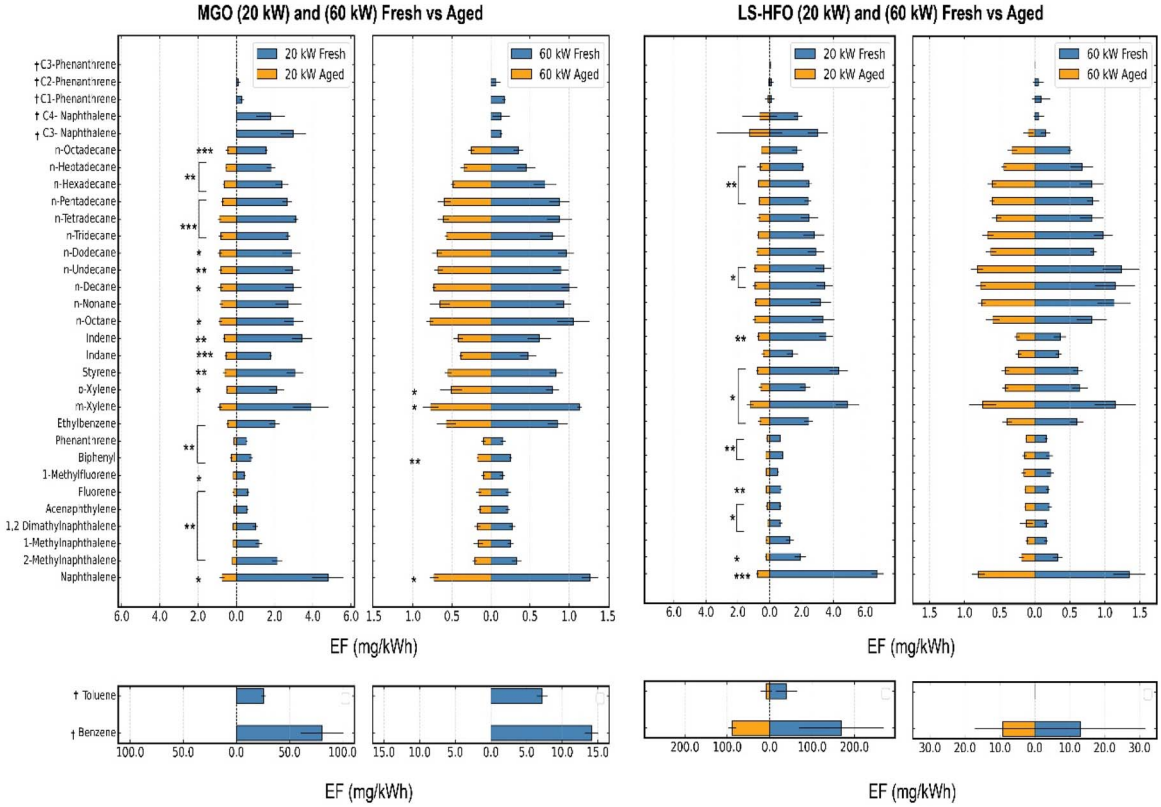

Fig. 4 Emission factors (EFs, F kWh^{-1}) of VOCs/IVOCSs before (blue) and after (orange) photochemical aging at low (20 kW) and high (60 kW) engine loads for MGO (left) and LS-HFO (right) (arithmetic mean ± standard deviation). For TD-GCMS compounds: $n = 4$ and 3 for 20 and 60 kW fresh and aged samples of MGO, and $n = 3$ for each fresh and aged samples of LS-HFO. For REMPI-TOF-MS compounds: $n = 3$ and 2 for 20 and 60 kW fresh and aged samples of MGO, $n = 2$ and 3 for 20 and 60 kW fresh and aged samples of LS-HFO. Asterisks indicating the level of significance based upon the adjusted p-value after Bonferroni corrections have been illustrated next to bars. *** for $p < 0.001$, ** for $p < 0.01$ and * for $p < 0.05$, bars without significant values have no asterisks. The adjusted p-values for all the compounds are provided in the SI (S11 and S12).

80-kW) was observed; nevertheless, SOA formation was higher at lower ones (Table S16).

PCA was conducted to investigate the relationship between the VOCs/IVOCs emission pattern and the fuel-type, engine load and aging conditions. Prior to PCA, all targeted VOCs/IVOCs were normalized relative to their total concentration. Fig. 5a–c shows the score plots illustrating the sample similarities, according to the experimental factors. The loading plot (Fig. 5d) provides insights into which VOC/IVOC species contribute to the scattering and clustering of the samples in the score plots. The relative majority of the total variance was found to be a consequence of differences between aromatics and aliphatics. Additionally, there was a vertical separation that distinguished monoaromatics from polyaromatics, while no distinct property among the aliphatics was observed. However, this pattern was not directly reflected in score plots with factors like fuel-type, aging condition or engine load, emphasizing that the observed chemical profile was shaped by interactions between these factors, rather than the additive effects of individual factors. During photochemical aging, both aromatics and aliphatics decreased in concentration. However, aromatics underwent more substantial depletion due to their higher reaction kinetics with OH·. This results in a relatively higher share of aliphatics in aged samples, despite the decline in their own absolute concentration. Fresh samples at 60 kW (negative PC1) are characterized by a lower VOC/NO_x ratio, so the limited availability of OH· for VOC reactions due to competition with NO_x reduces the extent of photochemical transformation compared to 20 kW. The lack of significant separation between the fuels suggests that the ship VOC/IVOC emissions followed a general pattern, regardless of fuel type but stronger effect by engine load.

The insights from PCA analysis are not only crucial for understanding the behavior of VOC/IVOC emissions under different conditions, but can also provide support for source apportionment studies. A study by Anders *et al.* (2024)[53] utilized PCA to differentiate fuel-dependent emission signatures from ships, and highlighted the potential of alkylation pattern of PAHs as fuel-specific markers in source apportionment studies using single-particle mass spectrometry. Traditional source apportionment methods, such as positive matrix factorization (PMF), may be inaccurate, as it assumes constant source profiles, ignoring dilution and photochemical losses. Studies by Yang *et al.* (2022)[54] and Liu *et al.* (2023)[55] have demonstrated that uncorrected PMF results often underestimate the contributions from reactive VOC sources like biogenic emissions or

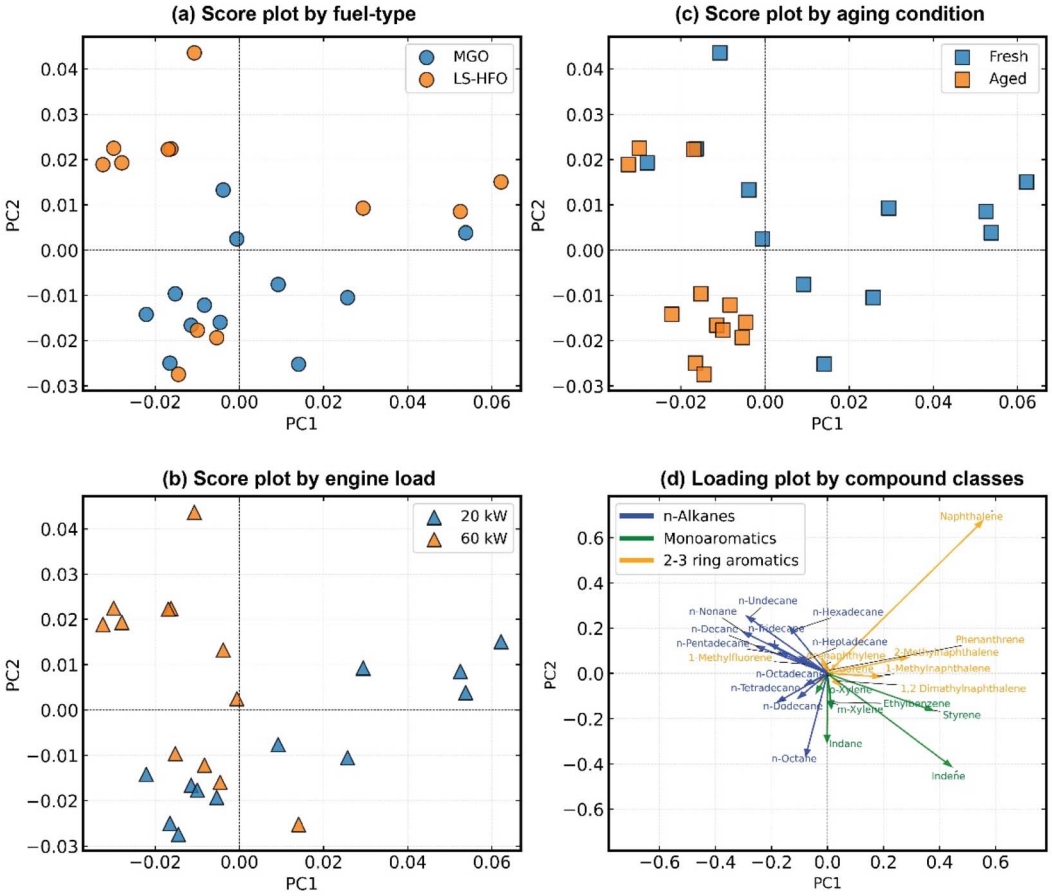

Fig. 5 Principal Component Analysis (PCA) representing the score plots by (a) fuel-type (MGO *vs.* LS-HFO), (b) engine load (20 kW Vs 60 kW), (c) condition (fresh *vs.* aged), and (d) loading plot focusing on different precursor classes.

gasoline-related compounds due to their depletion during atmospheric transport. Integrating reaction kinetics or photochemical corrections into PMF or in general receptor models[54] address this limitation by restoring the initial concentrations of reactive species.

3.3 SOA formation from the photooxidation of VOC/IVOC precursors

The SOA formation potential was estimated using bottom-up estimations, *i.e.*, VOCs oxidation yield method, by utilizing literature SOA yields of specific precursors. The SOA yield is highly dependent on the availability of oxidants, organic aerosol loading and NO_x availability.[56] NO_x availability modifies the chemical pathways of the reaction intermediates in the atmosphere. In general, high NO_x (NMHC/NO_x < 2) leads to lower SOA yields for several VOCs/IVOCs.[57] However, it is important to acknowledge that the NO_x chemistry within an OFR differs significantly from ambient atmospheric conditions. Even under high NO_x levels, the reaction pathway of (RO_2 + NO) does not dominate in OFRs operating at a 254 nm wavelength. This is because NO is rapidly converted to NO_2 *via* reaction with O_3. Subsequently, through oxidation by OH·, it transforms into nitrate (NO_3^-). As a result, NO is unavailable to participate in the (RO_2 + NO) reaction pathway, which is a key process in urban or polluted air. Furthermore, the SOA yields of precursors also differ under varied settings; for example, the SOA yields from OH·/Cl-initiated oxidation of VOCs/IVOCs tend to increase as the carbon number increases for molecules with similar chemical structures.[58] Furthermore, the presence of seed aerosol (as condensation sink) also plays an important role, significantly enhancing SOA yields.[59]

SOA yields for monoaromatics, PAHs and alkylated PAHs and *n*-alkanes were selected based upon the available literature yields. Further details on yields for different precursor classes are documented in the SI Text S2. The estimated SOA varied in magnitude, ranging from 2.3–62 mg SOA kWh^{-1} from high (80 kW) to low load (20 kW) for MGO, and 2.4–61 mg SOA kWh^{-1} from high (80 kW) to low load (20 kW) for LS-HFO. These estimated SOA levels were relatively lower than the reported estimated SOA productions using MGO and LS-HFO for the auxiliary engine,[60] while they were in the range of the estimated SOA reported from a study focused on cargo ships with low-sulfur fuel.[39] The switching of fuel from high- to low-sulfur fuel had little influence compared to previous studies.[24,61]

The different VOC contents and their proportions in the emission profile, which is highly dependent on fuel properties, engine in-use and operating conditions, could lead to different

SOA estimations. Fig. S4 presents the contribution of different precursor classes to the estimated SOA mass in different loads. Monoaromatics consistently dominated the mass contribution across all the loads. SOA production at low load (20 kW) was the highest, and contributed around 64% and 70% of the total estimated SOA for MGO and LS-HFO, respectively. This is particularly concerning because ships typically operate at low-load conditions in ports or along inland rivers close to urban areas, which will inevitably result in greater SOA production in urban atmospheres.

3.4 Measured SOA *vs.* estimated SOA: investigation of mass balance closure

Photochemical aging led to extensive secondary particle formation as mass increased with extended photochemical exposure at lower loads. Measured SOA reached a maximum of 153 mg kWh^{-1} after equiv. photochemical aging of 3.8 days for MGO emissions at 20 kW engine load (Table S16). In the case of LS-HFO emissions, SOA formation reached a maximum of 180 mg kWh^{-1} after equiv. photochemical aging of 4.2 days at 20 kW engine load. Further details on fuel and engine load-dependent SOA mass formation are available in Table S16. Fig. 6a and b compares the estimated SOA formed from analyzed VOC/IVOC precursors to the online measured SOA by HR-TOF-AMS across different engine loads. The estimated SOA explained a substantial fraction of ~41% and ~32% of measured SOA at lower (20 kW and 40 kW, respectively) engine loads for MGO. In contrast, for LS-HFO, only ~34% and ~14% of the measured SOA could be explained by the estimated SOA formed from the targeted VOC/IVOC precursors at the same engine loads.

The considerable difference in total SOA formation across engine loads for LS-HFO underscores that the unexplained SOA may result from missing precursors because of the high complexity of the emissions affected by the unburned fuel. Rüger *et al.* (2017)[62] compared the fuel composition and aerosol emitted from a marine engine, and emphasized the fundamental differences in oxidation pathways and chemical evolution of aerosols from HFO and diesel oil. Although the aromatics analyzed with TD-GCMS and REMPI-TOF-MS exhibit high SOA yields, additional compounds in the complex LS-HFO may contribute to SOA formation, but were not accounted for and not included in the target list. The observed discrepancies between the measured and estimated SOA for both fuels prompted further investigation into the underlying secondary particle formation mechanism.

Freshly emitted MGO aerosol particles exhibit a bimodal distribution, with significant fractions of particles in the nucleation mode (below 50 nm) and in the accumulation mode (50–100 nm). Aging facilitated both nucleation, where gas-phase precursors formed both new small particles, and condensation, where oxidized vapor phase species condensed onto existing particles leading to growth (Fig. 6c). This combination of

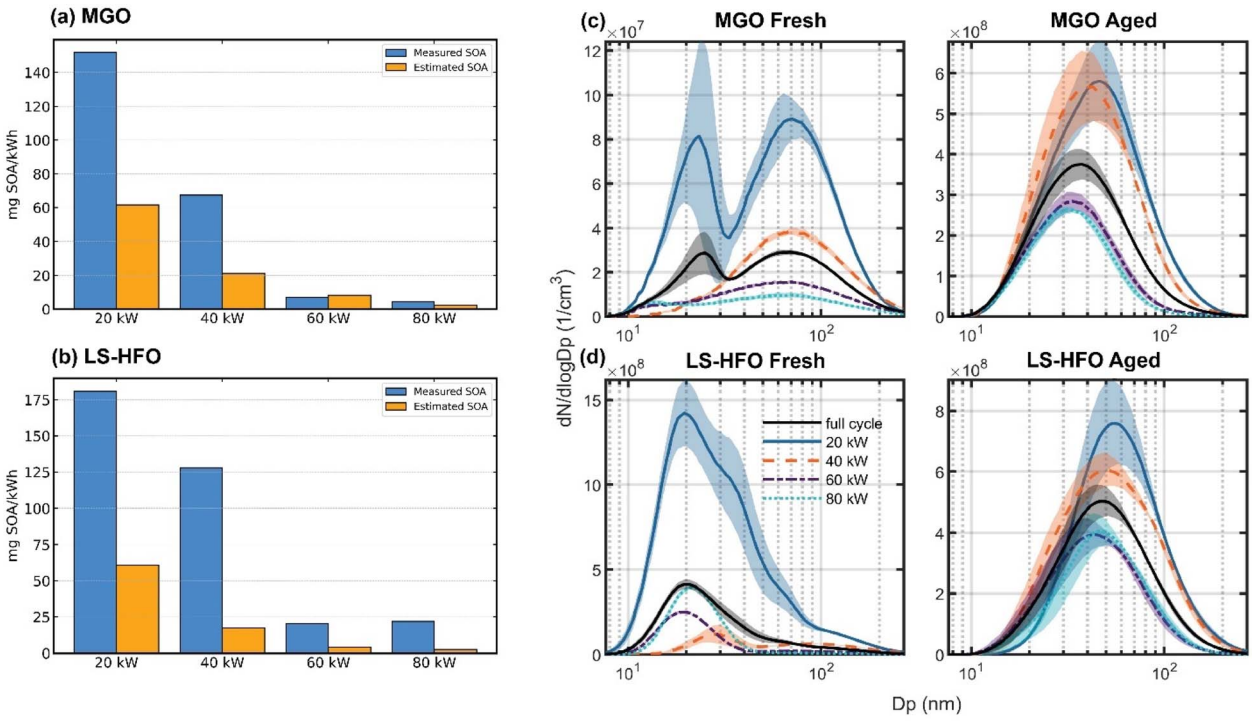

Fig. 6 Estimated SOA production from VOCs/IVOCs oxidation using bottom-up estimation in 20-, 40-, 60-, and 80 kW engine loads for MGO (a and c) and LS-HFO (b and d). The contribution of different precursor classes to SOA formation is presented in Fig. S4. (c and d) Present the particle size distribution at 20, 40, 60, and 80 kW engine load, as well as for the full cycle (2 hours) in black. The shaded area around the line presents the standard error of the mean (s.e.m.). The data for the total particle number concentration (N [cm^{-3}]), geometric mean diameter (GMD) and mode (Dp [nm]) are available in Table S17.

nucleation and condensation is evident from the enhanced total particle number concentration in aged emissions compared to fresh emissions, with a notable increase in smaller nucleation mode (mode1) presented in Table S17. In contrast, for LS-HFO emissions (Fig. 6d), there is a shift in mode diameter from ~20 nm to ~48 nm after aging, accompanied by an increase in the total particle number concentration. The growth of larger particles might be a combination of coagulation and condensation-driven growth, which is also supported by the particle size (GMD), as documented in Table S17.

3.5 Limitations

It is important to acknowledge that, despite the discrepancy between the estimated SOA based on precursors and the actual measured SOA for MGO and LS-HFO, the uncertainties associated with the SOA estimation method remain the same for both fuels. First, the SOA yields used for these estimations are derived from smog chamber experiments. While these experiments account for particle losses to chamber walls, they often do not account for vapor losses, which could result in a potential underestimation of the SOA yield. Second, the provided bottom-up estimate does not account for subsequent oxidation of reacted compounds or the interaction between different species.[63] Third, certain oxygenated volatile species, and cyclic IVOCs, such as cyclic alkanes and alkenes with substantial contribution in total marine engine emissions, could not be measured due to instrumental limitations. Intermediate volatility long chain alkanes (C12–C22) play a significant role in SOA formation,[64] and studies have shown that including these species narrows the gap between the observed and modeled SOA yields.[64,65] In addition, the OFR itself and the applied aging conditions could result in some uncertainties by a combination of factors, such as the condensation sink and NO_x concentration, leading to under- or over-estimation. Peng and Jimenez (2020)[66] highlighted that the elevated oxidative environment in the OFRs often promotes non-standard radical production processes. Moreover, NO_x chemistry inside the reactor can present unique challenges due to non-tropospheric radical reactions that can alter the expected chemistry pathways.

Regarding particle formation and growth, it is crucial to consider that nucleation, condensation, coagulation/agglomeration, fragmentation, and heterogeneous reactions operate on different timescales within the OFR compared to ambient atmosphere. In our OFR experiments, elevated concentrations promote faster coagulation/agglomeration, while the short residence time limits the extent of these processes, as compared to real atmospheric conditions with the same OH exposure. The motivation of using OFR in our study is to achieve equiv. photochemical ages beyond approximately 1.5 days, which are hardly accessible by the environmental chamber, making them very useful for modeling atmospheric processes. High concentrations of oxidants in OFR may cause more intense homogeneous oxidation in the gas phase than under ambient conditions, potentially leading to different product formation and a more enhanced formation of nucleation mode particles than in the atmosphere. The relatively short residence time of 1–2 min in the reactor may be insufficient for completion of RO_2 reaction pathways, and oxidized vapors may not fully condense, which may then leave the OFR in the gas phase. A modeling study on toluene OFR-aging[67] revealed that SOA yields may be substantially underestimated when the reactor residence is short and no seed aerosol is available to act as a condensation sink. However, fresh particle emissions offset the latter effect in our study. Furthermore, the bulk and molecular physical–chemical properties of OFR- and chamber-aged toluene-SOA were significantly different, but small on an absolute scale, thus supporting OFR-aging as an atmospheric processing model.

Quantitative particle measurements may be affected by wall losses inside the PEAR, but were minimized by conductive stainless-steel walls, laminar flow, and a relatively low surface-to-volume ratio (16.4 m^{-1}), and have been described in detail in a previous publication by Ihalainen *et al.* (2019).[26] For vapor losses, the condensation sink for combustion aerosols at similar conditions was found relatively high (>0.07 s^{-1}). Hence, the condensation onto aerosol particles dominated the molecular flux of low volatile organics, resulting in <2.1% wall losses for different experiments and OH· exposure cases. Hartikainen *et al.* (2020)[68] also investigated the fate of LVOCs in the PEAR for wood combustion aerosols under similar conditions, and reported negligible wall losses for different equivalent days of photochemical aging. Overall, wall losses are a minor contributor to the uncertainty of the experimental results.

It is also important to consider that the uncertainties associated with quantification are bi-directional, as AMS encounters challenges[69] in accurately measuring nucleation mode particles. For particles of smaller size, transmission is reduced due to insufficient inertia to maintain a focused trajectory, resulting in dispersion due to Brownian motion. A comparison of the integrated SMPS-derived volume-size distributions above 60 nm with the total size indicates the coverage of the AMS, which is 63–85% for HFO and 83–92% for MGO, depending on the engine load. This limitation in transmission efficiency underestimates the SOA formation. However, since the particle mass changes by the cube of the particle diameter, small particles not captured by the AMS due to low transmission only negligibly contribute to the particle mass of the aged aerosol. Assuming a particle density of 1.5 g cm^{-3}, a balance of non-refractory particle constituents and refractive Black Carbon (BC) with the SMPS-derived mass concentration can be found elsewhere.[51]

4 Conclusions

Marine engine emissions are directly influenced by fuel type and engine operating conditions. Our findings indicate that monoaromatics, particularly BTX compounds, were the predominant contributors to the overall identified VOC emissions, while naphthalene and alkylated naphthalenes were identified as the most abundant IVOC species. In the context of FSC regulations, the difference of LS-HFO and the SECA-compliant fuel MGO was relatively minor for most of the VOC/IVOC species. Thus, in contrast to particulate matter, additional measures on FSC do not provide an indirect benefit

of lower VOC/IVOC emissions. For most of the VOCs/IVOCs, the engine load was more important for the emission profile and EF than the fuel. Particularly low load conditions lead to enhanced emissions of unburned fuel and high EF, whereas higher loads revealed a larger fraction and EF of NO_x, also with consequences for the degradation of VOCs/IVOCs.

The photochemical aging process significantly decreased SOA precursors with a larger reduction over 3.8 ± 0.2 and 4.2 ± 0.7 equiv. days of aging at 20 kW for MGO and LS-HFO, respectively. Owing to their different OH· reactivity, aromatic VOCs/IVOCs were more degraded than the aliphatic emission constituents. Hence, photochemical aging alters the emission pattern of ship emissions, which may be considered in source apportionment studies. Furthermore, the formation of SOA was observed after photochemical aging for both fuels, and particularly for the two engine loads, which could be explained to a substantial extent by the SOA formation potential of targeted SOA precursors. However, it turned out that likely important SOA precursors are still missing, especially for LS-HFO, towards an accurate SOA formation prediction.

Existing studies on VOCs/IVOCs are insufficient to capture the full extent of marine emissions, underscoring the need for future research to explore gaseous organic emissions from ships and their atmospheric evolution during the aging process, along with SOA formation. This will be crucial for developing effective strategies to address the indirect benefits and unintended negative consequences of the IMO sulfur reduction policy.

Author contributions

DS: writing – original draft, writing – review & editing, visualization, investigation, formal analysis, and data curation; HC: writing – original draft, writing – review & editing, supervision, and formal analysis; TK: writing – review & editing, visualization, investigation, formal analysis, and data curation; MB: investigation, formal analysis, and data curation; AP: writing – review & editing, investigation, and formal analysis; UE: writing – review & editing, validation, methodology, investigation, formal analysis, and data curation; MI: validation, investigation, methodology, and data curation; ZF: writing – review & editing, methodology, and investigation; AH: formal analysis; NG: writing – review & editing and supervision; TH: writing – review & editing and supervision; YR: supervision; TS: writing – review & editing, project administration, funding acquisition, and conceptualization; BB: resources, funding acquisition, and conceptualization; OS: writing – review & editing, supervision, project administration, funding acquisition, and conceptualization; JØ: writing – review & editing, project administration, funding acquisition, and conceptualization; JSK: writing – review & editing and supervision; RZ: supervision, resources, project administration, funding acquisition, and conceptualization.

Conflicts of interest

There are no conflicts of interest to declare.

Data availability

The data supporting this article have been included as part of the SI.

Supplementary information includes measured data provided as an Excel file and details on the methodology and experimental setup. See DOI: https://doi.org/10.1039/d5ea00040h.

Acknowledgements

This research was supported by the EU Horizon 2020 project ULTRHAS – ULtrafine particles from TRansportation – Health Assessment of Sources, Grant Agreement No. 955390. Views and opinions expressed are those of the authors only and do not necessarily reflect those of the European Union. Neither the European Union nor the granting authority can be held responsible for them. H. C. acknowledges funding from Helmholtz International Lab "aeroHEALTH" (InterLabs-0005). We would like to thank Maxime Sueur (Université de Rouen Normandie, France) and Sandra Piel (University of Rostock) for their support during the campaign.

References

1 UNCTAD, Review of Maritime Report 2021, 2021, http://unctad.org/en/PublicationsLibrary/rmt2015_en.pdf.
2 OECD, *Ocean Shipping and Ship Building*, OECD, Boulogne-Billancourt, France, 2023, https://www.oecd.org/ocean/topics/oceanshipping/.
3 Y. Zhang, S. D. Eastham, A. K. H. Lau, J. C. H. Fung and N. E. Selin, Global air quality and health impacts of domestic and international shipping, *Environ. Res. Lett.*, 2021, **16**(8), DOI: 10.1088/1748-9326/ac146b.
4 R. M. Otto Paul, M. Karl, J. Bieser, J. P. Jalkanen and L. Johansson, Urban population exposure to NOx emissions from local shipping in three Baltic Sea harbour cities - a generic approach, *Atmos. Chem. Phys.*, 2019, **19**(14), 9153–9179, DOI: 10.5194/acp-19-9153-2019.
5 M. Viana, P. Hammingh, A. Colette, *et al.*, Impact of maritime transport emissions on coastal air quality in Europe, *Atmos. Environ.*, 2014, **90**, 96–105, DOI: 10.1016/j.atmosenv.2014.03.046.
6 M. Sofiev, J. J. Winebrake, L. Johansson, *et al.*, Cleaner fuels for ships provide public health benefits with climate tradeoffs, *Nat. Commun.*, 2018, **9**(1), 1–12, DOI: 10.1038/s41467-017-02774-9.
7 J. J. Corbett, J. J. Winebrake, E. H. Green, P. Kasibhatla, V. Eyring and A. Lauer, Mortality from ship emissions: A global assessment, *Environ. Sci. Technol.*, 2007, **41**(24), 8512–8518, DOI: 10.1021/es071686z.
8 S. Oeder, T. Kanashova, O. Sippula, *et al.*, Particulate matter from both heavy fuel oil and diesel fuel shipping emissions show strong biological effects on human lung cells at realistic and comparable in vitro exposure conditions, *PLoS One*, 2015, **10**(6), 1–17, DOI: 10.1371/journal.pone.0126536.

9 N. Mueller, M. Westerby and M. Nieuwenhuijsen, Health impact assessments of shipping and port-sourced air pollution on a global scale: A scoping literature review, *Environ. Res.*, 2023, **216**(P1), 114460, DOI: 10.1016/j.envres.2022.114460.

10 S. P. Kiihamäki, M. Korhonen, J. Kukkonen, I. Shiue and J. J. K. Jaakkola, Effects of ambient air pollution from shipping on mortality: A systematic review, *Sci. Total Environ.*, 2024, **945**, 173714, DOI: 10.1016/j.scitotenv.2024.173714.

11 C. Huang, Q. Hu, H. Wang, *et al.*, Emission factors of particulate and gaseous compounds from a large cargo vessel operated under real-world conditions, *Environ. Pollut.*, 2018, **242**, 667–674, DOI: 10.1016/j.envpol.2018.07.036.

12 T. Streibel, J. Schnelle-Kreis, H. Czech, *et al.*, Aerosol emissions of a ship diesel engine operated with diesel fuel or heavy fuel oil, *Environ. Sci. Pollut. Res.*, 2017, **24**(12), 10976–10991, DOI: 10.1007/s11356-016-6724-z.

13 Z. Shi, S. Endres, A. Rutgersson, *et al.*, Perspectives on shipping emissions and their impacts on the surface ocean and lower atmosphere: An environmental-social-economic dimension, *Elementa*, 2023, **11**(1), DOI: 10.1525/elementa.2023.00052.

14 A. L. Robinson, N. M. Donahue, M. K. Shrivastava, *et al.*, Rethinking organic aerosols: Semivolatile emissions and photochemical aging, *Science*, 2007, **315**(5816), 1259–1262, DOI: 10.1126/science.1133061.

15 C. A. Kontovas, Integration of air quality and climate change policies in shipping: The case of sulphur emissions regulation, *Mar. Policy*, 2020, **113**, 103815, DOI: 10.1016/j.marpol.2020.103815.

16 E. W. Carr and J. J. Corbett, Ship Compliance in Emission Control Areas: Technology Costs and Policy Instruments, *Environ. Sci. Technol.*, 2015, **49**(16), 9584–9591, DOI: 10.1021/acs.est.5b02151.

17 IMO, https://www.imo.org/en/OurWork/Environment/Pages/Nitrogen-oxides-(NOx)---Regulation-13.aspx, accessed February 3, 2025.

18 D. A. Lack, C. D. Cappa, J. Langridge, *et al.*, Impact of fuel quality regulation and speed reductions on shipping emissions: Implications for climate and air quality, *Environ. Sci. Technol.*, 2011, **45**(20), 9052–9060, DOI: 10.1021/es2013424.

19 M. Tauchi, K. Yamaji, R. Nakatsubo, *et al.*, Evaluation of the effect of Global Sulfur Cap 2020 on a Japanese inland sea area, *Case Stud. Transp. Pol.*, 2022, **10**(2), 785–794, DOI: 10.1016/j.cstp.2022.02.006.

20 N. M. Donahue, J. H. Kroll, S. N. Pandis and A. L. Robinson, A two-dimensional volatility basis set-Part 2: Diagnostics of organic-aerosol evolution, *Atmos. Chem. Phys.*, 2012, **12**(2), 615–634, DOI: 10.5194/acp-12-615-2012.

21 R. Tang, Q. Lu, S. Guo, *et al.*, Measurement report: Distinct emissions and volatility distribution of intermediate-volatility organic compounds from on-road Chinese gasoline vehicles: Implication of high secondary organic aerosol formation potential, *Atmos. Chem. Phys.*, 2021, **21**(4), 2569–2583, DOI: 10.5194/acp-21-2569-2021.

22 Z. Wu, Y. Zhang, J. He, *et al.*, Dramatic increase in reactive volatile organic compound (VOC) emissions from ships at berth after implementing the fuel switch policy in the Pearl River Delta Emission Control Area, *Atmos. Chem. Phys.*, 2020, **20**(4), 1887–1900, DOI: 10.5194/acp-20-1887-2020.

23 L. Huang, H. Liu, G. Yarwood, *et al.*, Modeling of secondary organic aerosols (SOA) based on two commonly used air quality models in China: Consistent S/IVOCs contribution but large differences in SOA aging, *Sci. Total Environ.*, 2023, **903**, DOI: 10.1016/j.scitotenv.2023.166162.

24 C. Huang, Q. Hu, Y. Li, *et al.*, Intermediate Volatility Organic Compound Emissions from a Large Cargo Vessel Operated under Real-World Conditions, *Environ. Sci. Technol.*, 2018, **52**(21), 12934–12942, DOI: 10.1021/acs.est.8b04418.

25 R. Tang, S. Guo, K. Song, *et al.*, Emission characteristics of intermediate volatility organic compounds from a Chinese gasoline engine under varied operating conditions: Influence of fuel, velocity, torque, rotational speed, and after-treatment device, *Sci. Total Environ.*, 2024, **906**, 167761, DOI: 10.1016/j.scitotenv.2023.167761.

26 M. Ihalainen, P. Tiitta, H. Czech, *et al.*, A novel high-volume Photochemical Emission Aging flow tube Reactor (PEAR), *Aerosol Sci. Technol.*, 2019, **53**(3), 276–294, DOI: 10.1080/02786826.2018.1559918.

27 L. Mueller, G. Jakobi, H. Czech, *et al.*, Characteristics and temporal evolution of particulate emissions from a ship diesel engine, *Appl. Energy*, 2015, **155**, 204–217, DOI: 10.1016/j.apenergy.2015.05.115.

28 O. Sippula, B. Stengel, M. Sklorz, *et al.*, Particle emissions from a marine engine: Chemical composition and aromatic emission profiles under various operating conditions, *Environ. Sci. Technol.*, 2014, **48**(19), 11721–11729, DOI: 10.1021/es502484z.

29 B. Yuan, A. R. Koss, C. Warneke, M. Coggon, K. Sekimoto and J. A. De Gouw, Proton-Transfer-Reaction Mass Spectrometry: Applications in Atmospheric Sciences, *Chem. Rev.*, 2017, **117**(21), 13187–13229, DOI: 10.1021/acs.chemrev.7b00325.

30 A. Allani, Y. Bedjanian, D. K. Papanastasiou and M. N. Romanias, Reaction Rate Coefficient of OH Radicals with d9-Butanol as a Function of Temperature, *ACS Omega*, 2021, **6**(28), 18123–18134, DOI: 10.1021/acsomega.1c01942.

31 Y. C. Mason, G. L. Schoonraad, J. Orasche, *et al.*, Comparative sampling of gas phase volatile and semi-volatile organic fuel emissions from a combustion aerosol standard system, *Environ. Technol. Innov.*, 2020, **19**, 100945, DOI: 10.1016/j.eti.2020.100945.

32 T. Streibel and R. Zimmermann, Resonance-enhanced multiphoton ionization mass spectrometry (REMPI-ms): Applications for process analysis, *Annu. Rev. Anal. Chem.*, 2014, **7**, 361–381, DOI: 10.1146/annurev-anchem-062012-092648.

33 P. F. DeCarlo, J. R. Kimmel, A. Trimborn, *et al.*, Field-deployable, high-resolution, time-of-flight aerosol mass

spectrometer, *Anal. Chem.*, 2006, **78**(24), 8281–8289, DOI: 10.1021/ac061249n.

34 J. T. Jayne, D. C. Leard, X. Zhang, *et al.*, Development of an aerosol mass spectrometer for size and composition analysis of submicron particles, *Aerosol Sci. Technol.*, 2000, **33**(1–2), 49–70, DOI: 10.1080/027868200410840.

35 E. Hartner, A. Paul, U. Käfer, *et al.*, On the Complementarity and Informative Value of Different Electron Ionization Mass Spectrometric Techniques for the Chemical Analysis of Secondary Organic Aerosols, *ACS Earth Space Chem.*, 2022, **6**(5), 1358–1374, DOI: 10.1021/acsearthspacechem.2c00039.

36 A. H. Hartikainen, S. Basnet, P. Yli-Pirilä, *et al.*, Resolving emission factors and formation pathways of organic gaseous compounds from residential combustion of European brown coal, *Combust. Flame*, 2024, **265**, 113485, DOI: 10.1016/j.combustflame.2024.113485.

37 G. A. Lavole, J. B. Heywood and J. C. Keck, Experimental and theoretical study of nitric oxide formation in internal combustion engines, *Combust. Sci. Technol.*, 1970, **1**(4), 313–326, DOI: 10.1080/00102206908952211.

38 Y. Zhao, K. Cui, J. Zhu, *et al.*, Effects of retarding fuel injection timing on toxic organic pollutant emissions from diesel engines, *Aerosol Air Qual. Res.*, 2019, **19**(6), 1346–1354, DOI: 10.4209/aaqr.2019.03.0112.

39 F. Zhang, B. Xiao, Z. Liu, *et al.*, *Real-World Emission Characteristics of VOCs from Typical Cargo Ships and their 1 Potential Contributions to SOA and O3 under Low-Sulfur Fuel Policies 2*, published online, 2024, pp. 8999–9017.

40 C. Huang, Q. Hu, Y. Li, *et al.*, Intermediate Volatility Organic Compound Emissions from a Large Cargo Vessel Operated under Real-World Conditions, *Environ. Sci. Technol.*, 2018, **52**(21), 12934–12942, DOI: 10.1021/acs.est.8b04418.

41 Z. Liu, Y. Chen, Y. Zhang, *et al.*, Emission Characteristics and Formation Pathways of Intermediate Volatile Organic Compounds from Ocean-Going Vessels: Comparison of Engine Conditions and Fuel Types, *Environ. Sci. Technol.*, 2022, **56**(18), 12917–12925, DOI: 10.1021/acs.est.2c03589.

42 E. S. Cross, A. G. Sappok, V. W. Wong and J. H. Kroll, Load-Dependent Emission Factors and Chemical Characteristics of IVOCs from a Medium-Duty Diesel Engine, *Environ. Sci. Technol.*, 2015, **49**(22), 13483–13491, DOI: 10.1021/acs.est.5b03954.

43 H. Czech, B. Stengel, T. Adam, M. Sklorz, T. Streibel and R. Zimmermann, A chemometric investigation of aromatic emission profiles from a marine engine in comparison with residential wood combustion and road traffic: Implications for source apportionment inside and outside sulphur emission control areas, *Atmos. Environ.*, 2017, **167**, 212–222, DOI: 10.1016/j.atmosenv.2017.08.022.

44 C. Radischat, O. Sippula, B. Stengel, *et al.*, Real-time analysis of organic compounds in ship engine aerosol emissions using resonance-enhanced multiphoton ionisation and proton transfer mass spectrometry Aerosols and Health, *Anal. Bioanal. Chem.*, 2015, **407**(20), 5939–5951, DOI: 10.1007/s00216-015-8465-0.

45 C. Huang, Q. Hu, Y. Li, *et al.*, Intermediate Volatility Organic Compound Emissions from a Large Cargo Vessel Operated under Real-World Conditions, *Environ. Sci. Technol.*, 2018, **52**(21), 12934–12942, DOI: 10.1021/acs.est.8b04418.

46 Z. Liu, Y. Chen, Y. Zhang, *et al.*, Emission Characteristics and Formation Pathways of Intermediate Volatile Organic Compounds from Ocean-Going Vessels: Comparison of Engine Conditions and Fuel Types, *Environ. Sci. Technol.*, 2022, **56**(18), 12917–12925, DOI: 10.1021/acs.est.2c03589.

47 M. Cui, Y. Xu, Z. Liu, *et al.*, Characteristics of intermediate volatility organic compounds emitted from inland vessels with different influential factors and implication of reduction emissions, *Sci. Total Environ.*, 2023, **904**, 166868, DOI: 10.1016/j.scitotenv.2023.166868.

48 E. C. Tuazon, S. M. Aschmann and R. Atkinson, Atmospheric degradation of volatile methyl-silicon compounds, *Environ. Sci. Technol.*, 2000, **34**(10), 1970–1976, DOI: 10.1021/es9910053.

49 X. Wu, X. Yao, B. Xie, *et al.*, Unraveling the atmospheric oxidation mechanism and kinetics of naphthalene: Insights from theoretical exploration, *Chemosphere*, 2024, **352**, 141356, DOI: 10.1016/j.chemosphere.2024.141356.

50 A. W. H. Chan, K. E. Kautzman, P. S. Chhabra, *et al.*, Secondary organic aerosol formation from photooxidation of naphthalene and alkylnaphthalenes: Implications for oxidation of intermediate volatility organic compounds (IVOCs), *Atmos. Chem. Phys.*, 2009, **9**(9), 3049–3060, DOI: 10.5194/acp-9-3049-2009.

51 A. Paul, T. Kokkola, Z. Fang, *et al.*, The impact of photochemical aging on secondary aerosol formation from a marine engine, *npj Clim. Atmos. Sci.*, 2025, **8**(1), 106, DOI: 10.1038/s41612-025-00985-2.

52 P. Karjalainen, K. Teinilä, N. Kuittinen, *et al.*, Real-world particle emissions and secondary aerosol formation from a diesel oxidation catalyst and scrubber equipped ship operating with two fuels in a SECA area, *Environ. Pollut.*, 2022, **292**, DOI: 10.1016/j.envpol.2021.118278.

53 L. Anders, J. Schade, E. I. Rosewig, *et al.*, Polycyclic aromatic hydrocarbons as fuel-dependent markers in ship engine emissions using single-particle mass spectrometry, *Environ. Sci.: Atmos.*, 2024, **4**(7), 708–717, DOI: 10.1039/d4ea00035h.

54 T. Yang, B. Liu, Y. Yang, Q. Dai, Y. Zhang and Y. Feng, Improved positive matrix factorization for source apportionment of volatile organic compounds in vehicular emissions during the Spring Festival in, *Environ. Pollut.*, 2022, **303**(38), 119122, DOI: 10.1016/j.envpol.2022.119122.

55 B. Liu, Y. Yang, T. Yang, Q. Dai, Y. Zhang and Y. Feng, Effect of photochemical losses of ambient volatile organic compounds on their source apportionment, *Environ. Int.*, 2023, **172**(38), 107766, DOI: 10.1016/j.envint.2023.107766.

56 D. Srivastava, T. V. Vu, S. Tong, Z. Shi and R. M. Harrison, Formation of secondary organic aerosols from anthropogenic precursors in laboratory studies, *npj Clim. Atmos. Sci.*, 2022, **5**(1), DOI: 10.1038/s41612-022-00238-6.

57 Z. Wan, K. Song, W. Zhu, *et al.*, A Closure Study of Secondary Organic Aerosol Estimation at an Urban Site of Yangtze River Delta, China, *Atmosphere*, 2022, **13**(10), 1–15, DOI: 10.3390/atmos13101679.

58 Y. B. Lim and P. J. Ziemann, Effects of molecular structure on aerosol yields from OH radical-initiated reactions of linear, branched, and cyclic alkanes in the presence of NO x, *Environ. Sci. Technol.*, 2009, **43**(7), 2328–2334, DOI: **10.1021/es803389s**.

59 E. Z. Nordin, A. C. Eriksson, P. Roldin, *et al.*, Secondary organic aerosol formation from idling gasoline passenger vehicle emissions investigated in a smog chamber, *Atmos. Chem. Phys.*, 2013, **13**(12), 6101–6116, DOI: **10.5194/acp-13-6101-2013**.

60 Z. Liu, Y. Chen, Y. Zhang, *et al.*, Emission Characteristics and Formation Pathways of Intermediate Volatile Organic Compounds from Ocean-Going Vessels: Comparison of Engine Conditions and Fuel Types, *Environ. Sci. Technol.*, 2022, **56**(18), 12917–12925, DOI: **10.1021/acs.est.2c03589**.

61 Z. Wu, Y. Zhang, J. He, *et al.*, Dramatic increase in reactive volatile organic compound (VOC) emissions from ships at berth after implementing the fuel switch policy in the Pearl River Delta Emission Control Area, *Atmos. Chem. Phys.*, 2020, **20**(4), 1887–1900, DOI: **10.5194/acp-20-1887-2020**.

62 C. P. Rüger, T. Schwemer, M. Sklorz, P. B. O'Connor, M. P. Barrow and R. Zimmermann, Comprehensive chemical comparison of fuel composition and aerosol particles emitted from a ship diesel engine by gas chromatography atmospheric pressure chemical ionisation ultra-high resolution mass spectrometry with improved data processing routines, *Eur. J. Mass Spectrom.*, 2017, **23**(1), 28–39.

63 C. L. Heald and J. H. Kroll, The fuel of atmospheric chemistry: Toward a complete description of reactive organic carbon, *Sci. Adv.*, 2020, **6**(6), 1–8, DOI: **10.1126/sciadv.aay8967**.

64 J. Li, K. Li, H. Li, *et al.*, Long-chain alkanes in the atmosphere: A review, *J. Environ. Sci.*, 2022, **114**, 37–52, DOI: **10.1016/j.jes.2021.07.021**.

65 B. Zhao, S. Wang, N. M. Donahue, *et al.*, Quantifying the effect of organic aerosol aging and intermediate-volatility emissions on regional-scale aerosol pollution in China, *Sci. Rep.*, 2016, **6**, 1–10, DOI: **10.1038/srep28815**.

66 Z. Peng and J. L. Jimenez, Radical chemistry in oxidation flow reactors for atmospheric chemistry research, *Chem. Soc. Rev.*, 2020, **49**(9), 2570–2616, DOI: **10.1039/c9cs00766k**.

67 H. Czech, P. Yli-Pirilä, P. Tiitta, *et al.*, The effect of aging conditions at equal OH exposure in an oxidation flow reactor on the composition of toluene-derived secondary organic aerosols, *Environ. Sci.: Atmos.*, 2024, **4**(7), 718–731, DOI: **10.1039/d4ea00027g**.

68 A. Hartikainen, P. Tiitta, M. Ihalainen, *et al.*, Photochemical transformation of residential wood combustion emissions: Dependence of organic aerosol composition on OH exposure, *Atmos. Chem. Phys.*, 2020, **20**(11), 6357–6378, DOI: **10.5194/acp-20-6357-2020**.

69 B. M. Matthew, A. M. Middlebrook and T. B. Onasch, Collection efficiencies in an aerodyne aerosol mass spectrometer as a function of particle phase for laboratory generated aerosols, *Aerosol Sci. Technol.*, 2008, **42**(11), 884–898, DOI: **10.1080/02786820802356797**.